Optimization of GaInNAs quantum-well vertical-cavity surface-emitting laser emitting at 2.33 µm

**Robert P. Sarzała · Łukasz Piskorski ·
Robert Kudrawiec · Włodzmierz Nakwaski**

Abstract In the present paper, a comprehensive computer simulation is used to determine optimal structure of the InP-based GaInNAs quantum-well (QW) active region and to investigate a possibility of reaching room-temperature (RT) continuous-wave (CW) single-fundamental-mode 2.33-µm operation of vertical-cavity surface-emitting laser (VCSEL) with such an active region. From among various considered InP-based active regions, the one with the $Ga_{0.15}In_{0.85}N_{0.015}As_{0.985}/Al_{0.138}Ga_{0.332}In_{0.530}As$ QW, i.e. with barriers lattice matched to InP, seems to be optimal for the 2.33-µm VCSEL performance. Its QW material is chosen for the required long-wavelength emission whereas its barrier is expected to ensure promising laser performance at room and higher temperatures. The latter is mostly connected with the QW conduction band offset equal in the above active region to as much as 413 meV, which is much larger than those of its possible lattice matched to InP competitors, e.g. 276 meV for the $Ga_{0.47}In_{0.53}As$ barrier and 346 meV for the $Ga_{0.327}In_{0.673}As_{0.71}P_{0.29}$ one. Our simulation reveals that from among various considered structures, a VCSEL with a 4-µm-diameter tunnel junction and two 6-nm $Ga_{0.15}In_{0.85}N_{0.015}As_{0.985}/Al_{0.138}Ga_{0.332}In_{0.530}As$ QWs exhibits the lowest calculated threshold current of 0.88 mA. Its promising RT CW performance suggests that it may represent a very interesting alternative to GaSb-based VCSELs.

R.P. Sarzała · Ł. Piskorski (✉) · W. Nakwaski
Photonics Group, Institute of Physics,
Lodz University of Technology, Wolczanska 219, 90-924 Lodz,
Poland
e-mail: lukasz.piskorski@p.lodz.pl
Fax: +48-42/631-3639

R. Kudrawiec
Institute of Physics, Wroclaw University of Technology,
Wybrzeze Wyspianskiego 27, 50-370 Wroclaw, Poland

1 Introduction

There is now increasing interest in the room-temperature (RT) continuous-wave (CW) regime of mid-infrared semiconductor devices due to their possible applications such as distant air monitoring, laser spectroscopy, medical diagnostics, thermovision measurements and wireless optical communication. Semiconductor lasers emitting radiation of wavelengths longer than 2 µm are currently grown on GaSb substrates [1]. However, their manufacturing is relatively expensive and complex and performance of these lasers is still far from the expected one. An alternate substrate material is InP [2], which is much cheaper than GaSb. Furthermore, InP-based devices can be manufactured using well-known, much simpler and less expensive technology. Therefore, there is a wide interest to replace in the above applications the GaSb lasers with the InP-based ones produced, for example, using diluted nitrides such as InNAs, GaInNAs and GaInNAsSb.

Dilute nitride alloys have some unusual properties in comparison with most of the known semiconductors [3]. An increase in their nitride content leads to reductions of both the lattice constant and the energy gap [4]. Therefore, by choosing properly the mole fractions of indium and nitrogen, the strain within these nitride structures and their band gaps can be controlled as far as the layer thickness remains below a critical limit for creation of misfit dislocations. In GaAs-based vertical-cavity surface-emitting lasers (VCSELs), their application enables reaching both the 1.31-µm and the 1.55-µm emission bands [5] used in fiber optical communication. With the advanced InP-based technology, on the other hand, it seems to be possible to reach even the 3.5 µm emission. An attempt to reach in an InP-based laser long-wavelength emission (>2 µm) has just been published [2].
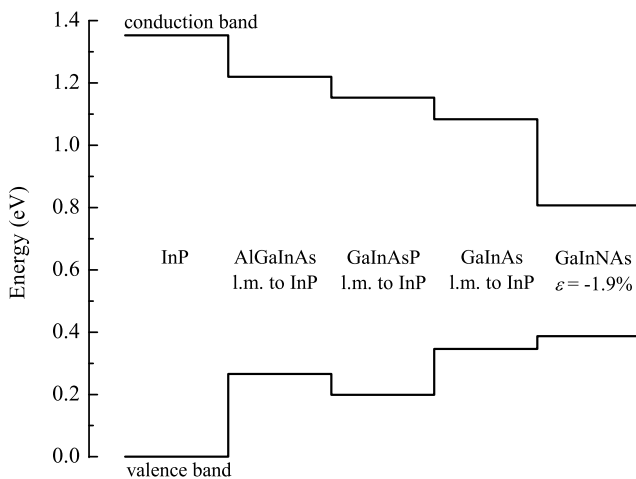
Fig. 1 RT energy-band alignments calculated for: the InP substrate, three barriers, i.e. the $Ga_{0.327}In_{0.673}As_{0.71}P_{0.29}$, $Al_{0.138}Ga_{0.332}In_{0.530}As$ and $Ga_{0.47}In_{0.53}As$ ones, lattice matched (l.m.) to InP and the compressively strained ($\varepsilon = -1.9$ %) $Ga_{0.15}In_{0.85}N_{0.015}As_{0.985}$ QW

In this paper we investigate a possibility of reaching RT CW single-fundamental-mode operation of 2.33 μm in InP-based GaInNAs quantum-well (QW) VCSELs. Because of strong absorption of this radiation by carbon monoxide (CO), such VCSELs may be used in distant detection of this poisonous gas. Generally, VCSEL devices are expected to exhibit remarkable properties such as single-longitudinal-mode operation, low-divergence circular output beam emission, high repeatability rate, wide wavelength tenability without mode hopping, low power consumption and low-cost mass production [6]. They are ideal light sources for a large number of applications such as optical communication or gas sensing where small laser powers are sufficient. First, in our comparative simulation we use the theoretical model described in our previous publication [2] to calculate the optical gain spectra. In our calculations, the following active-region structures emitting radiation of wavelengths longer than 2 μm with barriers lattice matched to InP have been considered: GaInNAs/GaInAsP, GaInNAs/AlGaInAs and GaInNAs/GaInAs strained QWs. Because of different band offsets of the above QW barrier materials (Fig. 1), different QW depths in their conduction and valence bands are obtained. After determination of the optimal QW structure, we use the fully self-consistent optical–electrical–thermal-recombination model to investigate the threshold characteristics of the possible 2.33-μm InP-based GaInNAs QW VCSEL.

2 Theoretical model

The comprehensive three-dimensional (3D) optical–electrical–gain–thermal self-consistent model of the 2.33-μm

InP-based GaInNAs QW VCSEL has been developed to investigate its threshold operation. The computer model consists of four interrelated parts:

- The finite-element (FE) electrical model characterizes the current spreading including carrier drift and diffusion processes within the device volume between the top and the bottom contacts, the injection of both electrons and holes into the active region, and their radial diffusion within it before their monomolecular, bimolecular and Auger recombinations.
- The FE thermal model gives details of heat generation in both non-radiative recombination and reabsorption of radiation as well as the volume and the barrier Joule heating and its spreading from the heat sources toward the heat sink and within it.
- The optical model describes, for successive radiation modes, optical fields within the resonator. The model is based on the effective frequency method [7]. The lasing threshold is determined from the condition of the real propagation constant.
- The gain model, based on Fermi's golden rule, gives information about the optical gain spectra. A brief description of the theoretical model for calculating the optical gain and electronic band structures of the strained QW active regions may be found in our previous publication [2].

Besides, all important, usually nonlinear, interactions between the above physical phenomena are taken into account. More details about the simulation model may be found in our previous publications, e.g. Refs. [8–11]. General rules of the advanced modeling of VCSEL operation were also formulated by Osiński and Nakwaski [12].

Electrical conductivities of semiconductor layers depend on their doping and free carrier concentration [13]. Their values are determined using experimental data reported in Refs. [14–34] and [26–31, 35], respectively. The rest of the electrical conductivities are taken from Refs. [36–40]. Contact resistances are assumed to be equal to that determined in Ref. [41]. The recombination coefficients, and the ambipolar diffusion coefficient used in the simulation, are taken from Ref. [42]. RT thermal conductivities of semiconductor layers are calculated from thermal resistivities for binaries given in Refs. [43–47] using interpolation formulas found in Ref. [48] and bowing parameters taken from Refs. [49–54]. Their temperature dependences and analogous expressions for α-Si, SiO_2 and copper may be found in Ref. [55]. Because of extremely thin QW layers, the whole active region is assumed to exhibit the thermal conductivity of the barriers. For the indium solder, we used the constant value taken from Ref. [56]. RT values and temperature dependences of the band parameters for binaries and the bowing coefficients used in the gain calculations are taken from Refs. [57–60]. Interpolation schemes for the ternary and quaternary alloys

are given in Refs. [61, 62]. The energy gap and the electron effective mass in GaInNAs are calculated using formulas taken from Refs. [63] and [2], respectively. The refractive indices are taken from Refs. [64–72]. The absorption coefficients of semiconductor layers are determined using experimental data reported in Refs. [73–78]. Absorption coefficients for α-Si and SiO$_2$ can be neglected [79, 80]. For the p^{++}-AlGaInAs/n^{++}-AlGaInAs tunnel junction (TJ), the absorption coefficients are assumed to be equal to 1000 cm^{-1} and 100 cm^{-1}, respectively. The latter value is also assumed for the absorption coefficient of the AlGaInAs barriers. RT values of all the material parameters discussed in this section are collected in Table 1.

3 Active-region design

The optimal active-region structure is expected to ensure low-threshold RT emission of the desired radiation, this time the radiation of wavelengths longer than 2 μm. Performance of the QW laser depends mostly on its QW active-region structure, which means on compositions and thicknesses of its layers. Besides, it may be modified by mechanical stresses possible within the QW structure and by changing the barrier material. In this section, an impact of parameters of the InP-based GaInNAs QW laser structure (including intentionally introduced stresses) and barrier material on an active region performance will be considered. In this way, an optimal QW active region for the laser emitting the mid-infrared long-wavelength radiation is expected to be determined.

As can be seen from Fig. 2, increases in the compressive strain (in this case it corresponds to an increase in indium mole fraction) and the nitrogen mole fraction y in the QW active region result in a considerable increase in the wavelength value for which the optical gain peak is observed.

Let us consider the compressively strained ($\varepsilon = -1.9$ %) single QW Ga$_{0.15}$In$_{0.85}$N$_{0.015}$As$_{0.985}$/Ga$_{0.327}$In$_{0.673}$As$_{0.71}$P$_{0.29}$ active region ($d_{QW} = 6$ nm) of the InP-based device for which the gain peak wavelength observed in Fig. 2 is close to 2.33 μm. Its RT band structure determined with the aid of the model presented in Ref. [2] is shown in Fig. 3a. Electron and hole energy QW states as well as depths of successive potential barriers are indicated. As one can see, two electron states as well as three heavy-hole states and one light-hole state are confined within the QW. The transition between the first QW electron (e1) and hole (hh1) states corresponds to the wavelength of about 2394 nm. This wavelength is much longer than possible wavelengths for analogous transitions between QW states in similar lasers grown on GaAs [5], which may enable manufacturing efficient laser sources emitting such a long-wavelength radiation.

Gain spectra, maximal gain and wavelength for the gain peak determined for the same QW active region ($d_{QW} =$

Table 1 RT values of electrical, thermal, optical and gain parameters used in the simulation of the 2.33-μm QW TJ-VCSEL

Electrical conductivity	
α-Si	3×10^{-3} Ω^{-1} m^{-1}
SiO$_2$	1×10^{-8} Ω^{-1} m^{-1}
n$^+$-Ga$_{0.47}$In$_{0.53}$As	122933 Ω^{-1} m^{-1}
n-InP	18354 Ω^{-1} m^{-1}
p-InP	607 Ω^{-1} m^{-1}
Tunnel junction	5 Ω^{-1} m^{-1}
n-GaAs	26436 Ω^{-1} m^{-1}
n-Al$_{0.90}$Ga$_{0.10}$As	2081 Ω^{-1} m^{-1}
n-GaAs substrate	68555 Ω^{-1} m^{-1}
Electrode	20 Ω^{-1} m^{-1}
Recombination and diffusion coefficients	
Monomolecular recombination	1×10^{-8} s^{-1}
Bimolecular recombination	4×10^{-10} cm^3 s^{-1}
Auger recombination	2.43×10^{-28} cm^6 s^{-1}
Ambipolar diffusion	10 cm^2 s^{-1}
Thermal conductivity	
α-Si	0.98 W m^{-1} K^{-1}
SiO$_2$	1.44 W m^{-1} K^{-1}
Ga$_{0.47}$In$_{0.53}$As	4.41 W m^{-1} K^{-1}
InP	68.03 W m^{-1} K^{-1}
Tunnel junction	4.13 W m^{-1} K^{-1}
Active region	4.05 W m^{-1} K^{-1}
GaAs	44.05 W m^{-1} K^{-1}
Al$_{0.90}$Ga$_{0.10}$As	25.53 W m^{-1} K^{-1}
Indium solder	84 W m^{-1} K^{-1}
Heat sink	400.8 W m^{-1} K^{-1}
Gain parameters	
QW energy gap	0.420 eV
QW depth in conduction band	0.413 eV
QW depth in valence band	0.121 eV
Waveguide depth in conduction band	0.133 eV
Waveguide depth in valence band	0.266 eV
Spin–orbit splitting	0.360 eV
Lorentz broadening	0.1 ps
QW refractive index	3.8
QW electron effective mass	$0.061 m_0$
QW heavy hole effective mass	$0.284 m_0$
QW light hole effective mass	$0.038 m_0$
Barrier electron effective mass	$0.050 m_0$
Barrier heavy hole effective mass	$0.318 m_0$
Barrier light hole effective mass	$0.079 m_0$

Table 1 (*Continued*)

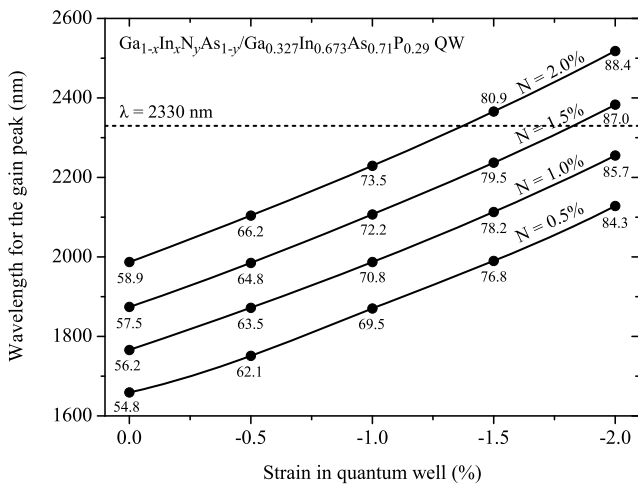| Optical parameters	Refractive index	Absorption coefficient
α-Si	3.6	$0\ \mathrm{cm^{-1}}$
SiO_2	1.433	$0\ \mathrm{cm^{-1}}$
n^+-$Ga_{0.47}In_{0.53}As$	3.2	$12\ \mathrm{cm^{-1}}$
n-InP	3.120	$1\ \mathrm{cm^{-1}}$
p-InP	3.120	$16\ \mathrm{cm^{-1}}$
p^{++}-$Al_{0.21}Ga_{0.26}In_{0.53}As$	3.405	$1000\ \mathrm{cm^{-1}}$
n^{++}-$Al_{0.21}Ga_{0.26}In_{0.53}As$	3.405	$100\ \mathrm{cm^{-1}}$
$Ga_{0.15}In_{0.85}N_{0.015}As_{0.985}$ QW	3.8	–
$Al_{0.138}Ga_{0.332}In_{0.530}As$ barrier	3.440	$100\ \mathrm{cm^{-1}}$
n-GaAs	3.328	$2.1\ \mathrm{cm^{-1}}$
n-$Al_{0.90}Ga_{0.10}As$	2.911	$6.9\ \mathrm{cm^{-1}}$

Fig. 2 RT gain peak wavelengths of the compressively strained 6-nm $Ga_{1-x}In_xN_yAs_{1-y}/Ga_{0.327}In_{0.673}As_{0.71}P_{0.29}$ QW active region determined for the active-region carrier concentration of $n = 4 \times 10^{18}\ \mathrm{cm^{-3}}$ and various strains ε and nitrogen mole fractions. Numbers below data points represent values of In content (in %) in GaInNAs

6 nm), the active-region carrier concentration $n = 4 \times 10^{18}\ \mathrm{cm^{-3}}$ and for various ambient temperatures T are plotted in Figs. 4a and 5. As expected, an increase in the active-region temperature is followed by a red shift of the whole gain spectrum and leads to lower optical gain values. Maximal optical gain of about $2425\ \mathrm{cm^{-1}}$ has been determined for about 2342 nm and of about $1826\ \mathrm{cm^{-1}}$ for about 2407 nm for temperatures equal to 300 K and 350 K, respectively.

Let us now consider the technologically simpler structures without the phosphorus within their barriers. One of such structures is the compressively strained ($\varepsilon = -1.9$ %) $Ga_{0.15}In_{0.85}N_{0.015}As_{0.985}/Ga_{0.47}In_{0.53}As$ QW. As one can see in Fig. 3b, this time the heavy-hole confinement is very weak due to a much smaller QW depth in the valence
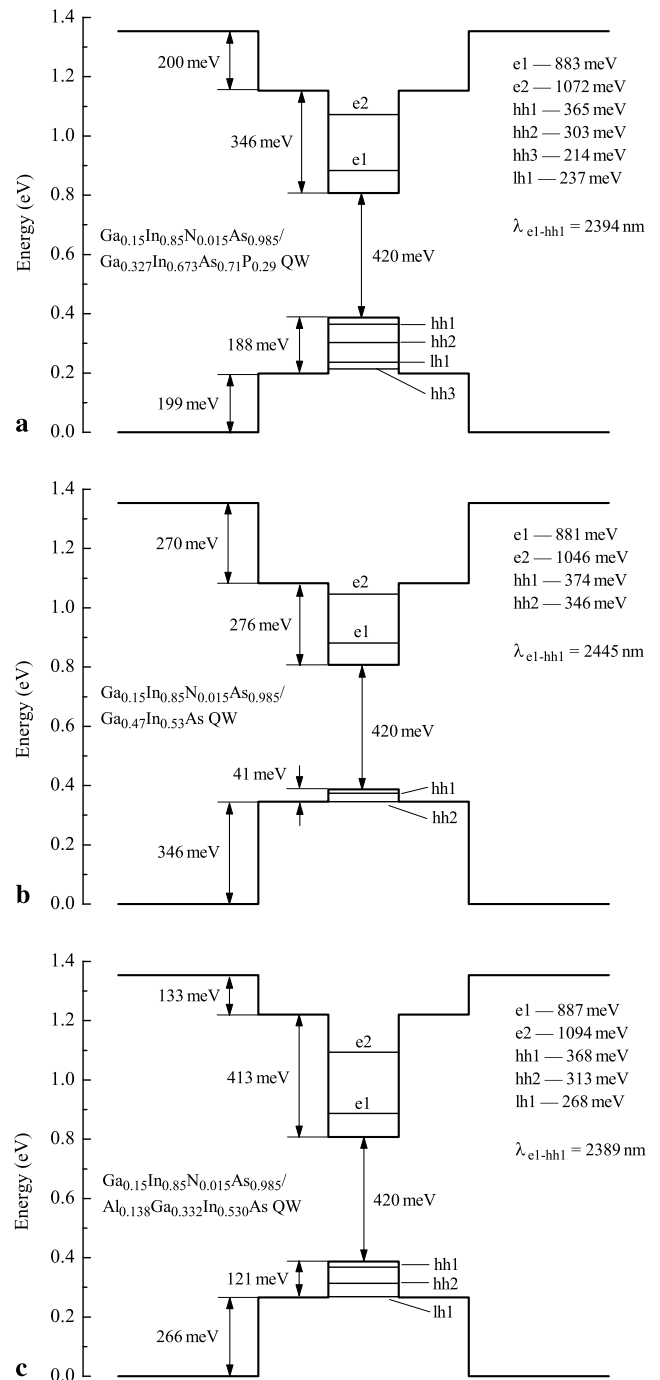

Fig. 3 RT band structures of the active regions with the compressively strained ($\varepsilon = -1.9$ %) 6-nm $Ga_{0.15}In_{0.85}N_{0.015}As_{0.985}$ QW and with following three barriers lattice matched to InP, i.e. (**a**) $Ga_{0.327}In_{0.673}As_{0.71}P_{0.29}$, (**b**) $Ga_{0.47}In_{0.53}As$, (**c**) $Al_{0.138}Ga_{0.332}In_{0.530}As$ barriers. The wavelength e1-hh1 determined for the transition between the first electron and heavy-hole levels is shown

band, which results in a lower number of hole QW energy states. The transition between the first QW electron (e1) and hole (hh1) states corresponds to the wavelength of about 2445 nm.
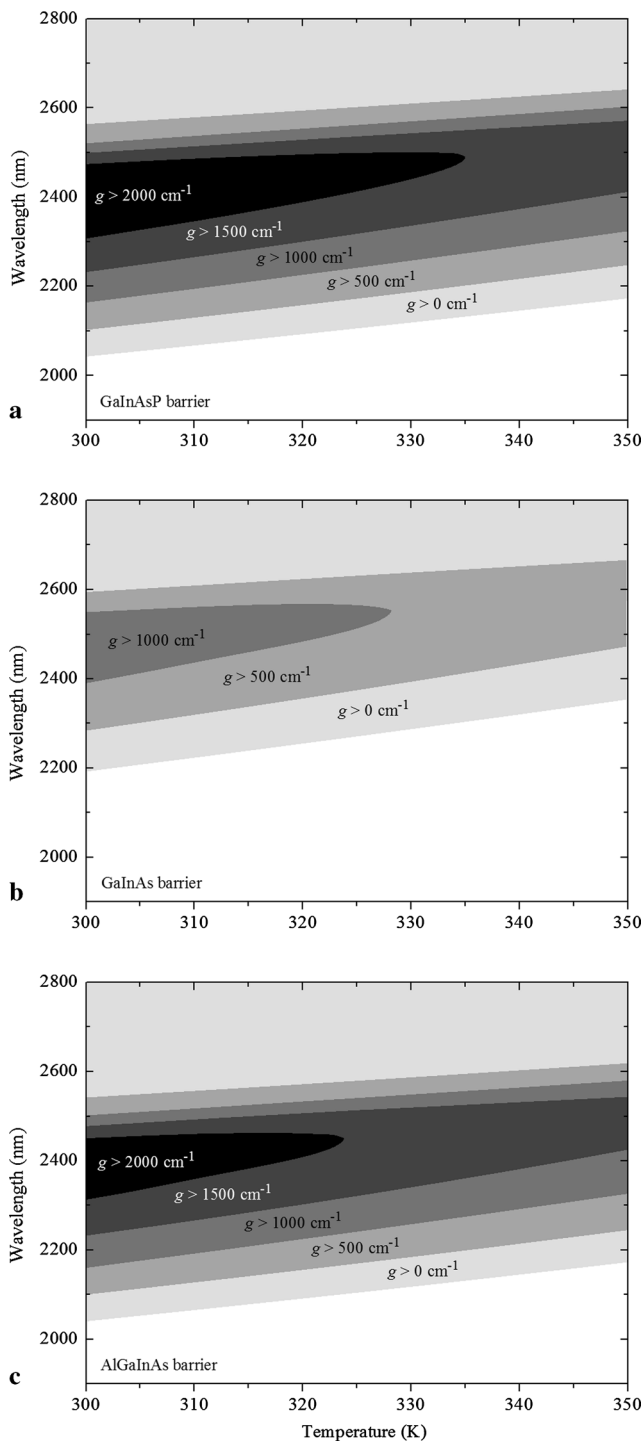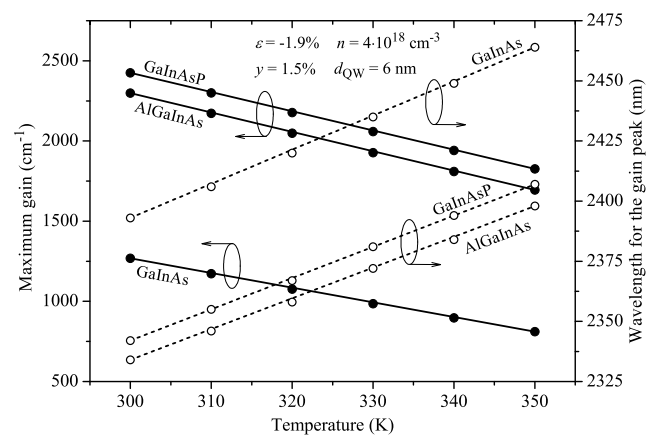
Fig. 5 Maximal gain and gain peak wavelength determined for various ambient temperatures T and for the active regions considered in this work

Fig. 4 Gain spectra of the compressively strained ($\varepsilon = -1.9$ %) 6-nm $Ga_{0.15}In_{0.85}N_{0.015}As_{0.985}$ QW and with the following three barriers lattice matched to InP, i.e. (**a**) $Ga_{0.327}In_{0.673}As_{0.71}P_{0.29}$, (**b**) $Ga_{0.47}In_{0.53}As$, (**c**) $Al_{0.138}Ga_{0.332}In_{0.530}As$ barriers determined for various active-region temperatures T and the active-region carrier concentration of $n = 4 \times 10^{18}$ cm^{-3}

Corresponding gain spectra, maximum gain and wavelength for the gain peak determined for the same QW active region ($d_{QW} = 6$ nm), the active-region carrier concentra- tion $n = 4 \times 10^{18}$ cm^{-3} and for various ambient tempera- tures T are plotted in Figs. 4b and 5. Maximal optical gain of about 1269 cm^{-1} has been determined for about 2393 nm and of about 811 cm^{-1} for about 2464 nm for temperatures equal to 300 K and 350 K, respectively. As can be seen, re- placing the GaInAsP barrier by the GaInAs one leads to the active region which offers a longer wavelength but, due to worse confinement for holes in the valence band, the offered optical gain is much lower.

Another possible active region without phosphorus is the compressively strained ($\varepsilon = -1.9$ %) $Ga_{0.15}In_{0.85}N_{0.015}$ $As_{0.985}/Al_{0.138}Ga_{0.332}In_{0.530}As$ QW. The number of the electron and heavy-hole energy states is the same as in the case of the $Ga_{0.15}In_{0.85}N_{0.015}As_{0.985}/Ga_{0.47}In_{0.53}As$ QW, but this time they are strongly confined due to a larger QW depth in both the conduction and valence bands (Fig. 3c). The transition between the first QW electron (e1) and hole (hh1) states corresponds to the wavelength of about 2389 nm and is comparable with the result obtained for the $Ga_{0.15}In_{0.85}N_{0.015}As_{0.985}/Ga_{0.327}In_{0.673}As_{0.71}P_{0.29}$ QW (Fig. 3a).

Corresponding gain spectra, maximal gain and wave- length for the gain peak determined for the same as the above QW active region ($d_{QW} = 6$ nm), the same active- region carrier concentration $n = 4 \times 10^{18}$ cm^{-3} and for var- ious ambient temperatures T are plotted in Figs. 4c and 5. This time, maximal optical gain of about 2299 cm^{-1} has been determined to take place for about 2334 nm and of about 1694 cm^{-1} for about 2398 nm for temperatures equal to 300 K and 350 K, respectively. As can be seen, the GaIn- NAs/AlGaInAs QW active region offers emission of radia- tion of almost the same wavelengths as those in the GaIn- NAs/GaInAsP QW. Gain spectra of this QW are shifted only by about 8 nm in comparison with those of the GaIn- NAs/GaInAsP QWs. The maximal gain values calculated for various temperatures for the GaInNAs/AlGaInAs QWs

are only slightly smaller than those observed for the GaIn-NAs/GaInAsP one, but the temperature impacts on their maximal gain values are very similar. That is why this non-phosphorus active region can be a very good alternative to the GaInNAs/GaInAsP QWs. Then this interesting and promising approach may be used to replace the InP claddings by the GaInAs ones lattice matched to InP. Then such a structure may be applied to eliminate P from the whole structure because such lasers can be grown in the same reactors as GaAs-based lasers.

Summarizing an influence of three different barriers on optical gain characteristics of GaInNAs QWs, it is clearly visible that the AlGaInAs barrier is a very promising solution in this case. Temperature sensitivities of the calculated gain peak wavelength and the maximal gain for the considered QW active region with the AlGaInAs barrier are equal to 1.28 nm/K and -12.1 cm^{-1} K^{-1}, respectively. These results are similar to analogous values of 1.30 nm/K and -12.0 cm^{-1} K^{-1} obtained for the GaInAsP barrier. For the GaInAs barrier, the calculated maximal gain sensitivity equal to -9.16 cm^{-1} K^{-1} is slightly smaller, but the analogous sensitivity of the gain peak wavelength of 1.43 nm/K is higher.

4 InP-based GaInNAs QW 2.33-μm VCSEL

In this section we investigate the threshold characteristics of the possible 2.33-μm InP-based QW VCSEL with the GaInNAs/AlGaInAs active region selected on the basis of the results from Sect. 3. The general concept of the modeled structure (Fig. 6) is similar to the currently most modern 2.33-μm GaInAsSb/AlGaAsSb GaSb-based VCSEL proposed in Refs. [81–83]. Its intentionally undoped active region is assumed to be composed of the 6-nm $Ga_{0.15}In_{0.85}N_{0.015}As_{0.985}$ QWs separated by the 10-nm $Al_{0.138}Ga_{0.332}In_{0.530}As$ internal barriers. External 30-nm barriers manufactured from the same material as the internal ones are assumed on both active-region edges. The
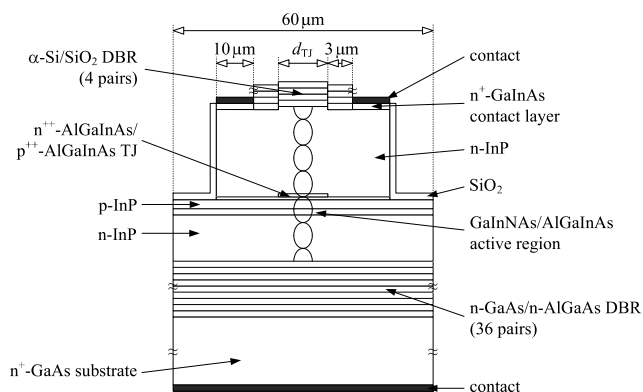
active region is sandwiched by InP spacers, doped with silicon (5×10^{17} cm^{-3}) or zinc (5×10^{17} cm^{-3}) on the n and p sides, respectively. Above the p-type spacer, the tunnel junction (TJ) composed of 15-nm p^{++}-$Al_{0.21}Ga_{0.26}In_{0.53}As$ doped with carbon (2×10^{19} cm^{-3}) and 15-nm n^{++}-$Al_{0.21}Ga_{0.26}In_{0.53}As$ doped with silicon (2×10^{19} cm^{-3}) is located. To minimize the absorption loss, the TJ is situated at the standing-wave node. The upper spacer is manufactured from InP doped with silicon up to 5×10^{17} cm^{-3}. The 3-λ cavity is terminated on both sides by distributed Bragg reflectors (DBRs): the four-pair α-Si (162 nm)/SiO$_2$ (407 nm) top DBR and the fused [84, 85] 36.5-pair GaAs (175 nm)/$Al_{0.90}Ga_{0.10}As$ (200 nm) bottom DBR. The bottom DBR is doped with silicon up to 2×10^{18} cm^{-3} ($Al_{0.90}Ga_{0.10}As$) and 5×10^{17} cm^{-3} (GaAs). The bottom DBR diameter is assumed to be equal to 60 μm, whereas the upper DBR diameter is larger by 6 μm than the TJ one. The top contact is produced in a form of a ring of 10-μm width. It is separated from the top spacer with the 200-nm-thick highly silicon-doped (5×10^{18} cm^{-3}) n$^+$-$Ga_{0.47}In_{0.53}As$ contact layer. The whole bottom 60-μm-diameter surface of the 200-μm GaAs substrate doped with silicon up to 2×10^{18} cm^{-3} is covered by the bottom contact. The laser is attached to the cylindrical (height = diameter = 5 mm) copper heat sink with 3-μm indium solder.

For an application of the considered VCSEL as a source of the carrier wave used in gas-sensing applications, it is of primary importance to obtain the stable single- fundamental-mode LP$_{01}$ emission. Although in the TJ-VCSELs, contrary to oxide-confined devices, it may be achieved even for large diameters, we restrict our discussion to TJs with small diameters for which, as will be shown later, threshold currents are relatively low. Wavelengths of the LP$_{01}$ modes as a function of the TJ diameter and a number of QWs are plotted in Fig. 7. For all calculated cases, the simulated laser shows

Fig. 6 The tunnel-junction (TJ) GaInNAs/AlGaInAs QW 2.33-μm VCSEL structure under consideration
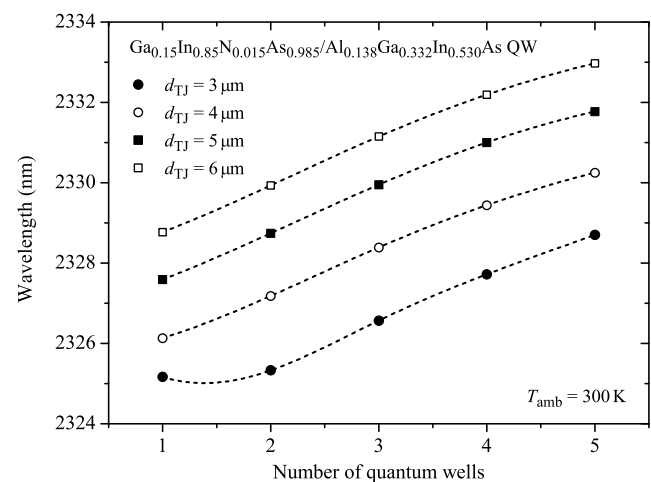

Fig. 7 RT dependence of the wavelength of CW emitted radiation as a function of the number of quantum wells determined for various tunnel-junction diameters d_{TJ} of GaInNAs/AlGaInAs QW 2.33-μm VCSEL
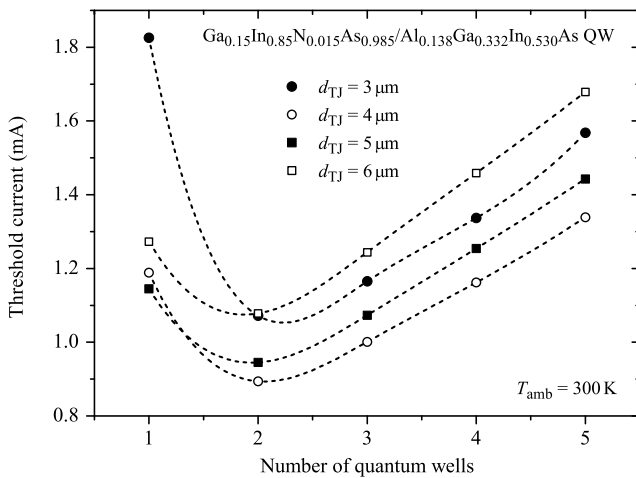
Fig. 8 RT dependence of the CW threshold current as a function of the number of quantum wells determined for various tunnel-junction diameters d_{TJ} of GaInNAs/AlGaInAs QW 2.33-µm VCSEL

Fig. 9 RT relative intensity distributions as a function of a distance r from the laser axis plotted for different TJ diameters d_{TJ} of GaInNAs/AlGaInAs QW 2.33-µm VCSEL

LP_{01} operation with emission wavelength close to 2.33 µm and can cover a strong absorption line of CO. In Fig. 7, a monotonic increase in lasing wavelength is observed. The reason is that the amplitude of the intensity within the active region is a slowly changing function of the position. Such behaviour originates in the interference of the standing wave. Any interface between two regions of different refractive indices contributes to the reflection of the wave. It is not the case if the interface coincides with an antinode of the wave. The observed change of the amplitude is triggered by the slight misalignment between interfaces of the QWs and the antinode of the wave, which is the expected effect.

Optimal structures of GaInNAs QW TJ-VCSELs have been determined by comparing their threshold currents (Fig. 8). For all TJ diameters d_{TJ}, the lowest thresholds have been found for two QWs. The threshold increase observed for single QWs follows from a too weak optical gain in such an active-region configuration. Then carriers of increasing concentration should be injected into the active region because of which the Auger recombination is increased, which is followed by an analogous increase in the lasing threshold. An increase in a number of QWs over two leads to a monotonic increase in VCSEL lasing threshold. An increased penetration of passive areas around QWs (Fig. 9) is a reason for the somewhat different behaviour of the curve plotted for the smallest TJ diameter, i.e. for $d_{TJ} = 3$ µm. Then this curve is distinctly shifted up as compared with the others.

5 Conclusion

The anticipated performance characteristics of InP-based GaInNAs QW active regions and a possibility of reaching
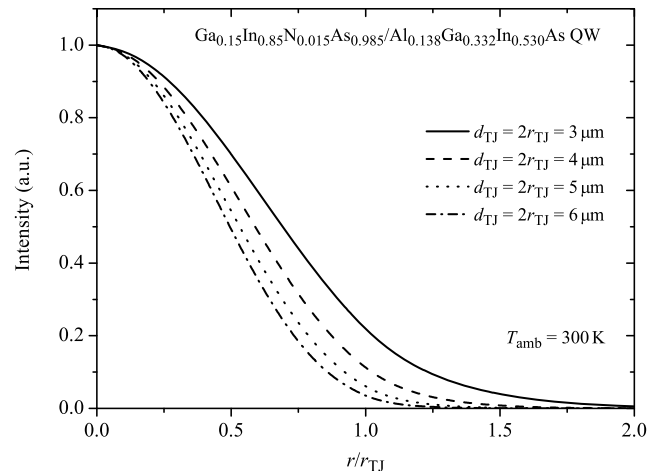
a RT CW single-fundamental-mode 2.33-µm lasing operation of a VCSEL with GaInNAs QWs have been investigated in the present paper with the aid of our comprehensive computer model. In the simulation, three different barrier materials lattice matched to InP have been selected to determine the optimal active-region structure for an efficient emission of the above long-wavelength radiation at various temperatures. Very good results have been obtained for the $Ga_{0.15}In_{0.85}N_{0.015}As_{0.985}/Al_{0.138}Ga_{0.332}In_{0.530}As$ active region, for which the conduction band offset equal to 413 meV is much larger than that of 276 meV for the $Ga_{0.47}In_{0.53}As$ barrier and that of 346 meV for the $Ga_{0.327}In_{0.673}As_{0.71}P_{0.29}$ one. The GaInNAs/AlGaInAs active region has been incorporated into the 2.33-µm VCSEL structure and the RT CW emission wavelengths and threshold currents have been calculated for various diameters of the TJ and various numbers of QWs. The results indicate that single-fundamental-mode operation of the above laser is possible. The lowest threshold current of 0.88 mA has been obtained for a VCSEL with a 4-µm-diameter TJ and two 6-nm GaInNAs/AlGaInAs QWs. The promising RT CW performance of the modeled 2.33-µm InP-based VCSEL with GaInNAs/AlGaInAs QWs suggests that it may represent a very interesting alternative to GaSb-based VCSELs.

References

1. Z. Yin, X. Tang, Solid-State Electron. **51**, 6 (2007)
2. R.P. Sarzała, Ł. Piskorski, P. Szczerbiak, R. Kudrawiec, W. Nakwaski, Appl. Phys. A **108**, 521 (2012)
3. M. Henini, *Dilute Nitride Semiconductors* (Elsevier, Oxford, 2005)
4. M. Kondow, K. Uomi, A. Niwa, T. Kitatani, S. Watahiki, Y. Yazawa, Jpn. J. Appl. Phys. **35**, 1273 (1996)
5. H.-P.D. Yang, C. Lu, R. Hsiao, C. Chiou, C. Lee, C. Huang, H. Yu, C. Wang, K. Lin, N.A. Maleev, A.R. Kovsh, C. Sung, C. Lai, J. Wang, J. Chen, T. Lee, J.Y. Chi, Semicond. Sci. Technol. **20**, 834 (2005)
6. F. Koyama, J. Lightwave Technol. **24**, 4502 (2006)
7. H. Wenzel, H.-J. Wünsche, IEEE J. Quantum Electron. **33**, 1156 (1997)
8. R.P. Sarzała, W. Nakwaski, J. Phys. Condens. Matter **16**, S3121 (2004)
9. R.P. Sarzała, Appl. Phys. A **81**, 275 (2005)
10. Ł. Piskorski, R.P. Sarzała, W. Nakwaski, Appl. Phys. A **98**, 651 (2010)
11. R.P. Sarzała, T. Czyszanowski, M. Wasiak, M. Dems, Ł. Piskorski, W. Nakwaski, K. Panajotov, Adv. Opt. Technol. **2012**, 689519 (2012)
12. M. Osiński, W. Nakwaski, *Vertical-Cavity Surface-Emitting Laser Devices* (Springer, Berlin, 2003)
13. H. Czichos, T. Saito, L.M. Smith, *Springer Handbook of Materials Measurement Methods* (Springer, Berlin, 2006)
14. T.F. Kuech, B.S. Meyerson, E. Veuhoff, Appl. Phys. Lett. **44**, 986 (1984)
15. J. Saito, K. Kondo, J. Vac. Sci. Technol. B **8**, 1264 (1990)
16. P.R. Hageman, M.H.J.M. de Croon, J.N.H. Reek, L.J. Giling, J. Cryst. Growth **116**, 169 (1992)
17. K. Tateno, C. Amano, J. Electron. Mater. **28**, 63 (1999)
18. V. Bondarenko, Positron annihilation study of equilibrium point defects in GaAs. Ph.D. thesis, Martin Luther University of Halle-Wittenberg (2003)
19. C. Blaauw, F.R. Shepherd, C.J. Miner, A.J. Springthorpe, J. Electron. Mater. **19**, 1 (1990)
20. J.N. Baillargeon, A.Y. Cho, R.J. Fischer, in *Proc. 6th Int. Conf. Indium Phosphide and Related Materials*, Santa Barbara, CA, 27–31 March (1994), p. 148
21. J.M. Milikow, Growth and characterization of III–V compound semiconductors. M.Sc. thesis, Massachusetts Institute of Technology (1997)
22. Ch. Giesen, X.G. Xu, R. Hövel, M. Heuken, K. Heime, in *Proc. 9th Int. Conf. Indium Phosphide and Related Materials*, Cape Cod, MA, 11–15 May (1997), p. 47
23. K. Radhakrishnan, H.Q. Zheng, P.H. Zhang, S.F. Yoon, G.I. Ng, J. Cryst. Growth **204**, 275 (1999)
24. F.G. Kellert, S.R. Sloan, J. Electron. Mater. **21**, 983 (1992)
25. B. Pődör, in *Proc. 31st Int. Spring Semin. Electronics Technology*, Budapest, 7–11 May (2008), p. 201
26. C.A.C. Sequeira, D.M.F. Santos, Braz. J. Phys. **38**, 147 (2008)
27. T. Ishikawa, J. Saito, S. Sasa, S. Hiyamizu, Jpn. J. Appl. Phys. **21**, L675 (1982)
28. M.L. Lovejoy, M.R. Melloch, M.S. Lundstrom, Appl. Phys. Lett. **67**, 1101 (1995)
29. S. Izumi, N. Hayafuji, K. Ito, K. Sato, M. Otsubo, Appl. Phys. Lett. **68**, 3102 (1996)
30. N. Chand, T. Henderson, J. Klem, W.T. Masselink, R. Fischer, Y.-C. Chang, H. Morkoc, Phys. Rev. B **30**, 4481 (1984)
31. N. Watanabe, T. Nittono, K. Watanabe, Appl. Phys. Lett. **61**, 1945 (1992)
32. K.Y. Cheng, A.Y. Cho, J. Appl. Phys. **53**, 4411 (1982)
33. R.A. Kubiak, J.J. Harris, P. Dawson, J. Appl. Phys. **55**, 598 (1984)
34. T. Fujii, T. Inata, K. Ishii, S. Hiyamizu, Electron. Lett. **22**, 191 (1986)
35. K. Beer, B. Baur, H. Heinecke, R. Treichler, J. Cryst. Growth **120**, 312 (1992)
36. P.G. Le Comber, J. Mort, *Electronic and Structural Properties of Amorphous Semiconductors* (Academic, New York, 1973)
37. J.F. Shackelford, W. Alexander, *CRC Materials Science and Engineering Handbook* (CRC, Boca Raton, 2001)
38. www.thinfilm.com
39. D.R. Lide, *CRC Handbook of Chemistry and Physics* (CRC, Boca Raton, 2005). Internet version
40. Ł. Piskorski, R.P. Sarzała, W. Nakwaski, Opto-Electron. Rev. **19**, 320 (2011)
41. O. Dier, C. Lauer, M.-C. Amann, Electron. Lett. **42**, 419 (2006)
42. P. Szczerbiak, The model of the diode laser emitting in the mid-infrared region with the dilute-nitride active region on indium phosphide substrate. B.Sc. thesis, Lodz University of Technology (2011) (in Polish)
43. E.F. Steigmeier, I. Kudman, Phys. Rev. **132**, 508 (1963)
44. I. Kudman, E.F. Steigmeier, Phys. Rev. **133**, A1665 (1964)
45. S. Amith, I. Kudman, E.F. Steigmeier, J. Appl. Phys. **138**, A1270 (1965)
46. E.F. Steigmeier, I. Kudman, Phys. Rev. **141**, 767 (1966)
47. M.A. Afromowitz, J. Appl. Phys. **44**, 1292 (1973)
48. W. Nakwaski, J. Appl. Phys. **64**, 159 (1988)
49. R. Bowers, J.E. Bauerle, A.J. Cornish, J. Appl. Phys. **30**, 1050 (1959)
50. M.S. Abrahams, R. Braunstein, F.D. Rosi, J. Phys. Chem. Solids **10**, 204 (1959)
51. B. Abeles, Phys. Rev. **131**, 1906 (1963)
52. R.O. Carlson, G.A. Slack, S.J. Silverman, J. Appl. Phys. **36**, 505 (1965)
53. W. Both, F.P. Herrmann, Cryst. Res. Technol. **17**, K117 (1982)
54. N. Yacoubi, B. Girault, J. Fesquet, Appl. Opt. **25**, 4622 (1986)
55. Ł. Piskorski, Modelling of the physical phenomena in the selected vcsel structures emitting at the second telecommunication window wavelength. Ph.D. thesis, Lodz University of Technology (2010) (in Polish)
56. www.lakeshore.com
57. I. Vurgaftman, J.R. Meyer, L.R. Ram-Mohan, J. Appl. Phys. **89**, 5815 (2001)
58. I. Vurgaftman, J.R. Meyer, J. Appl. Phys. **94**, 3675 (2003)
59. S. Wang, Phys. Status Solidi B **246**, 1618 (2009)
60. S. Adachi, *Properties of Semiconductor Alloys: Group-IV, III–V and II–VI Semiconductors* (Wiley, Chichester, 2009)
61. T.H. Glisson, J.R. Hauser, M.A. Littlejohn, C.K. Williams, J. Electron. Mater. **7**, 1 (1978)
62. C.K. Williams, T.H. Glisson, J.R. Hauser, M.A. Littlejohn, J. Electron. Mater. **7**, 639 (1978)
63. R. Kudrawiec, J. Appl. Phys. **101**, 023522 (2007)
64. www.refractiveindex.info
65. S. Gehrsitz, F.K. Reinhart, C. Gourgon, N. Herres, A. Vonlanthen, H. Sigg, J. Appl. Phys. **87**, 7825 (2000)
66. S. Adachi, Phys. Rev. B **35**, 7454 (1987)
67. S. Adachi, *Physical Properties of III–V Semiconductor Compounds* (Wiley, Chichester, 1992)
68. E. Kessels, Remote plasma deposition of hydrogenated amorphous silicon. Ph.D. thesis, Technische Universiteit Eindhoven (2000)
69. www.filmetrics.com
70. C. Grasse, G. Boehm, M. Mueller, T. Gruendl, R. Meyer, M.-C. Amann, Semicond. Sci. Technol. **25**, 045018 (2010)
71. B. Jensen, A. Torabi, J. Appl. Phys. **54**, 3623 (1983)
72. R.P. Sarzała, Ł. Piskorski, P. Szczerbiak, W. Nakwaski, R. Kudrawiec, in *Proc. European Materials Research, Society (E-MRS) Spring Meet.* Strasbourg, France, 14–18 May 2012 (2012), p. T-12

73. W.G. Spitzer, J.M. Whelan, Phys. Rev. **114**, 59 (1959)
74. D.I. Babic, J. Piprek, K. Streubel, R.P. Mirin, N.M. Margalit, D.E. Mars, J.E. Bowers, E.L. Hu, IEEE J. Quantum Electron. **33**, 1369 (1997)
75. O.K. Kim, W.A. Bonner, J. Electron. Mater. **12**, 827 (1983)
76. C.H. Henry, R.A. Logan, F.R. Merritt, J.P. Luongo, J. Quantum Electron. **19**, 947 (1983)
77. H.C. Casey, P.L. Carter, Appl. Phys. Lett. **44**, 82 (1984)
78. D.M. Wilt, N.S. Fatemi, P.P. Jenkins, V.G. Weizer, R.W. Hoffman Jr., R.K. Jain, Ch.S. Murray, D.R. Riley, NASA Tech. Memo. **113110**, 1 (1997)
79. M. Ortsiefer, C. Neumeyr, J. Rosskopf, S. Arafin, G. Böhm, A. Hangauer, J. Chen, R. Strzoda, M.-C. Amann, Proc. SPIE **7945**, 794509 (2011)
80. R. Kitamura, L. Pilon, M. Jonasz, Appl. Opt. **46**, 8118 (2007)
81. A. Bachmann, K. Kashani-Shirazi, S. Arafin, M.-C. Amann, IEEE J. Sel. Top. Quantum Electron. **15**, 933 (2009)
82. M.-C. Amann, S. Arafin, K. Vizbaras, Proc. SPIE **7952**, 795212 (2011)
83. S. Arafin, A. Bachmann, K. Vizbaras, A. Hangauer, J. Gustavsson, J. Bengtsson, A. Larsson, M.-C. Amann, Opt. Express **19**, 17267 (2011)
84. E. Kapon, Compd. Semicond. January–February **25** (2005)
85. A. Sirbu, N. Volet, A. Mereuta, J. Lyytikäinen, J. Rautiainen, O. Okhotnikov, J. Walczak, M. Wasiak, T. Czyszanowski, A. Caliman, Q. Zhu, V. Iakovlev, E. Kapon, Adv. Opt. Technol. **2011**, 209093 (2011)